ACS APPLIED MATERIALS & INTERFACES

www.acsami.org

Research Article

High Mobility Two-Dimensional Electron Gas at the $BaSnO_3/SrNbO_3$ Interface

Sharad Mahatara, Suresh Thapa, Hanjong Paik, Ryan Comes,* and Boris Kiefer*

Cite This: ACS Appl. Mater. Interfaces 2022, 14, 45025−45031

Read Online

ACCESS | Metrics & More | Article Recommendations | Supporting Information

ABSTRACT: Oxide two-dimensional electron gases (2DEGs) promise high charge carrier concentrations and low-loss electronic transport in semiconductors such as $BaSnO_3$ (BSO). ACBN0 computations for $BSO/SrNbO_3$ (SNO) interfaces show Nb-*4d* electron injection into extended Sn-*5s* electronic states. The conduction band minimum consists of Sn-*5s* states ~1.2 eV below the Fermi level for intermediate thickness 6-unit cell BSO/6-unit cell SNO superlattices, corresponding to an electron density in BSO of $\sim 10^{21}$ cm^{-3}. Experimental studies of analogous BSO/SNO interfaces grown by molecular beam epitaxy confirm significant charge transfer from SNO to BSO. In situ angle-resolved X-ray photoelectron spectroscopy studies show an electron density of $\sim 4 \times 10^{21}$ cm^{-3}. The consistency of theory and experiments show that BSO/SNO interfaces provide a novel materials platform for low loss electron transport in 2DEGs.

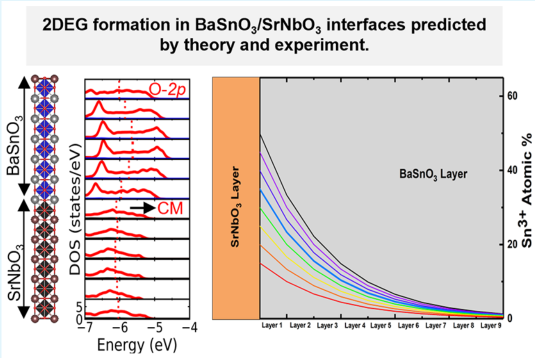

KEYWORDS: *2DEGS, charge transfer, electron density, heterostructure, conduction band minimum*

INTRODUCTION

Complex oxide interfaces are well known for hosting a two-dimensional electron gas (2DEG) as a result of band engineering, a property which is absent in the corresponding bulk compounds.[1,2] An oxide 2DEG was first observed in $LaAlO_3/SrTiO_3$ (LAO/STO) heterostructures consisting of two wide band gap insulators LAO (E_g = 5.5 eV, ref 3) and STO (E_g = 3.2 eV, ref 4). The 2DEG has carrier density ($\sim 10^{13}$ cm^{-2}),[5] strong confinement to the interface (~2 nm width),[6] and relatively high mobility at low temperatures ($\sim 10^5$ cm^2/Vs),[2] which makes it suitable for low-temperature electronic and optoelectronic applications.[7] Previously, defect engineering,[8] strain engineering,[9] and doping engineering[10] have been used to improve room-temperature mobility. In parallel, novel heterostructures, such as $NdAlO_3$/STO,[11] $NdTiO_3$/STO,[12] and $LaTiO_3$/STO,[13] have been developed, but their room-temperature charge carrier mobility is sub-optimal due to the presence of localized Ti-*3d* orbitals in STO that are strongly scattered by longitudinal optical phonons.[14]

An alternative approach is to design oxide heterostructures with a conduction band minimum (CBM) that is dominated by less localized s-orbitals, thereby increasing band dispersion and carrier mobility.[15,16] $BaSnO_3$ (BSO) with a Sn-*5s* dominated CBM is an excellent candidate for the rational design of 2DEG heterostructures.[15] With a Hall mobility as high as 320 cm^2 V^{-1} s^{-1}, BSO has the highest room-temperature mobility in complex metal oxides to date with an electron concentration of 8×10^{19} cm^{-3} in a La-doped bulk BSO single crystal.[17] One of the synthesis challenges for BSO 2DEG formation is the prevention of band filling and compensating defects that occur at high dopant concentrations.[18−20] The second challenge is to select a suitable material for electron injection into BSO. Previous density functional theory (DFT) studies for metallic $SrNbO_3$ (SNO)[21,22] show Nb-*4d* t_{2g} bands crossing the Fermi level and a large energy separation between O-*2p* and Nb-*4d* bands. These findings suggest possibly a large driving force for Nb-*4d* electron injection into BSO, and the realization of a 2DEG in the vicinity of BSO/SNO interfaces.

Here, we use the synergy of self-consistent Hubbard-U DFT computations with experimental synthesis and spectroscopy to explore the electronic structure of BSO/SNO heterostructures. The consistency of the DFT results with our X-ray photoelectron spectroscopy (XPS) experiments on MBE-grown heterostructures strongly suggests the presence of a high-mobility and high-density 2DEG at the BSO/SNO interface.

METHODS

Computations. All computations were performed within the framework of 3D-periodic DFT and complemented by a self-consistent Hubbard-U approach (ACBN0),[23−26] compatible with

Received: July 8, 2022
Accepted: September 2, 2022
Published: September 23, 2022

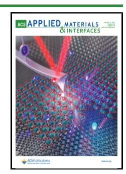

Quantum Espresso.[27,28] Following previous work,[29] ACBN0 Hubbard-U parameters were computed with norm-conserving pseudopotentials available in AFLOWπ[24] and combined with the projector augmented wave (PAW) scheme[30] and pseudopotentials from the ps 1.0.0 library,[31] for all subsequent computations. Electronic exchange and correlation effects were described within the Generalized Gradient Approximation (GGA) as parametrized in Perdew-Burke-Ernzerhof (PBE) functional,[32] using a plane wave energy cutoff of E_{cut} = 70 Ry (for further details see the Supporting Information). For cubic BSO and SNO crystal structures, we used the DFT equilibrium structures to determine self-consistent ACBN0 Hubbard-U parameters ($BaSnO_3$: Ba = 3.96 eV, Sn = 0.04 eV, O = 8.88 eV; $SrNbO_3$: Sr = 0.05 eV, Nb = 1.07 eV, O = 7.39 eV), similar to previously reported Hubbard-U values for perovskite oxides.[33] With these Hubbard-U parameters, we obtained an equilibrium lattice parameter for cubic BSO, a = 4.118 Å (SNO: 4.044 Å), comparable to our DFT relaxed lattice parameter of 4.178 Å (SNO: 4.061 Å), and in excellent agreement with the experiment, 4.115 Å[34] (SNO: 4.020 Å[35]). The BSO band gap increases from 0.4 eV (DFT) to 3.6 eV (ACBN0), closer to the experimental band gap of 3.1 eV,[36] while SNO remains non-magnetic metal, consistent with previous theory[35] and experiment.[37] We built different (BSO)N/(SNO)M heterostructures (N, M refer to the number of cubic unit cells in each stack): (BSO)4/(SNO)2, (BSO)4/(SNO)4, (BSO)6/(SNO)6, (BSO)7/(SNO)7, and (BSO)8/(SNO)8. The cross-sectional area and vertical dimensions of the heterostructures were fixed at the ACBN0 equilibrium lattice parameter of the BSO substrate, following previous work,[16,38,39] leading to an in-plane 1.8% tensile strain in the SNO layer. With these computational settings, we computed converged electronic structures and electronic density of states. The charge carrier density was computed by integrating the electronic density of states between the Fermi energy and an energy in the gap below the CBM. We computed the effective mass at the CBM, from fourth-order polynomial fits of the band dispersion along the M−Γ−X direction, following previous work.[40] Moreover, we computed the average charge density along the [001] stacking direction to address charge transfer localization in the heterostructures, following previous work.[41]

Experiments. The BSO/SNO heterostructure was created by growing SNO on as-prepared BSO (001) single-crystal films synthesized at Cornell University on Nb-doped STO (001) and $GdScO_3$ (110) substrates. SNO was synthesized at Auburn University using the hybrid molecular beam epitaxy (hMBE) approach described elsewhere using the tris(diethylamino)(t-butylimido)niobium (TBTDN) precursor.[22] SNO film thicknesses were between three and five unit cells in all cases to permit XPS measurements of the buried interface. Approximately, three unit cells of $SrHfO_3$ (SHO) was deposited as a capping layer in some cases to preserve the surface during cooldown based on our previous observations of the surface stability of SNO.[41] In-situ RHEED (Staib Instrument) was used to monitor the growth process and the quality of the film (for more details see the Supporting Information). One challenge for films grown on Nb:STO is that strain relaxation in BSO produces a rougher initial surface compared to a bare substrate. Films grown on strained BSO below the critical thickness on $GdScO_3$ demonstrated smoother surfaces and a sharper RHEED pattern. For this work, we focus our analysis on three samples: a bare 10 nm BSO film on Nb-doped STO, an uncapped 4-unit cell SNO film on a 25 nm BSO film on Nb-doped STO, and an SHO-capped 4-unit-cell SNO film on a 3 nm BSO film on $GdScO_3$. After growth, samples were transferred from the MBE reactor to a PHI 5400 XPS (Al Kα X-ray source, pressure ∼1 × 10^{-9} Torr) system through an ultra-high vacuum transfer line. Angle-resolved XPS (ARXPS) experiments were used to characterize the reduction of tin oxidation state from 4+ to 3+. An electron neutralizer gun was applied for compensating the charging of the insulating samples.[42] Analysis of the ARXPS data was performed using CasaXPS.[43,44] *Ex situ* atomic force microscopy measurements were carried out on an uncapped sample to check the morphology of SNO film (see Supporting Information, Figure S3).

■ RESULTS AND DISCUSSION

The properties of (BSO)/(SNO) (001) interfaces were investigated by varying the number of cubic unit cells in the BSO(N) and/or SNO(M) layers and we considered: (BSO)4/(SNO)2, (BSO)4/(SNO)4, (BSO)6/(SNO)6, (BSO)7/(SNO)7, and (BSO)8/(SNO)8. For (BSO)6/(SNO)6, our computations predict the highest downward shift of the CBM relative to the Fermi level (∼1.2 eV, Figure 1); and following

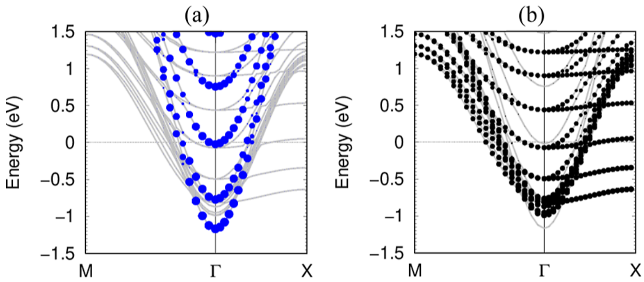

Figure 1. Orbital projected bandstructure of (BSO)6/(SNO)6 heterostructure: (a) Sn-5s and (b) Nb-4d.

ref 44, we estimate a carrier concentration of ∼10^{21} cm^{-3}. All other heterostructures have smaller downward shifts, indicating lower charge carrier densities (Figure S1 and Table S1 in the Supporting Information). Similarly, except for (BSO)8/(SNO)8, the CBM consists of Sn-5s electronic states, leading to an effective mass m^* of 0.104 m_0 (m_0, electron rest mass), very similar to BSO bulk (m^* = 0.098 m_0). Moreover, the effective mass varies by less than ∼6% among these heterostructures (Table S1 in the Supporting Information) and is ∼4 times lower than that of the known 2DEG hosting LAO/STO (001) heterostructure, m^* = 0.4 m_0.[45] In contrast, for the (BSO)8/(SNO)8 heterostructure, we find a ∼65% increase of the effective mass (Figure S1 and Table S1 in the Supporting Information) that is attributed to Nb-4d electronic states at the CBM. Therefore, our results confirm the hypothesized design principle of utilizing Sn-5s orbitals to increase mobile carrier concentration at BSO/SNO interfaces, facilitating 2DEG formation. The layer-resolved CBM for the (BSO)6/(SNO)6 heterostructure (Figure 2) shows that the CBM of the BSO layers (Sn-5s) is ∼0.2 eV below the CBM of the SNO layers (Nb-4d) consistent with charge transfer from SNO to BSO.

A high electron charge carrier density of ∼10^{21} cm^{-3} for the (BSO)6/(SNO)6 heterostructure is corroborated by the computed charge density variation perpendicular to the heterostructure stacking direction, [001] (Figure 2). The charge density in the BSO layer corresponds to an electron density of ∼10^{21} cm^{-3} per unit cell, while electron densities are ∼10× higher in the SNO layer. Moreover, the charge density in the SNO layer (1.3 × 10^{22} cm^{-3} per unit cell) corresponds closely to the charge density inferred for complete depletion of Nb-d^1 states (1e^- = 1.4 × 10^{22} cm^{-3}), supporting near-optimal charge transfer. Lastly, high electron accumulation at the (BSO)6/(SNO)6 interface is confirmed by the layer-resolved variation of the O-2p center-of-mass (CM). The VBM in bulk SNO consists of O-2p states and is located −5.2 eV below the Fermi energy (Figure S2 in the Supporting Information), similar to previous ARPES experiments that reported −4.4 eV,[45] while the O-2p CM is located ∼3.0 eV below the VBM, −7.4 eV below the Fermi energy. In contrast, the O-2p CM of

https://doi.org/10.1021/acsami.2c12195
ACS Appl. Mater. Interfaces 2022, 14, 45025−45031

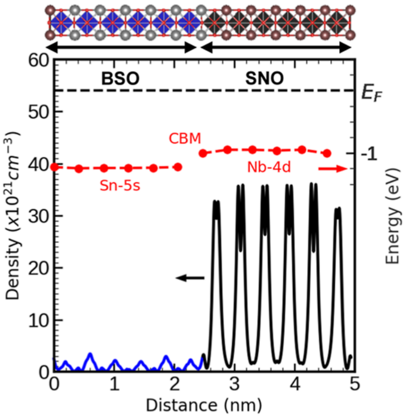

Figure 2. Planar average charge densities in (BSO)6/(SNO)6 plotted along the [001] direction, blue line: BSO; black line: SNO. Layer-resolved CBM for (BSO)6/(SNO)6 are shown as filled red circles.

BSO is located −2.6 eV below the Fermi energy, ∼4.8 eV higher as compared to bulk SNO (Figure S2 in the Supporting Information), generating the driving force for SNO to BSO charge transfer:[46] O-2*p* CM alignment leads to a shifted Fermi level in SNO that is more positive than that of BSO. The thermodynamic requirement of a well-defined and unique Fermi level throughout the heterostructure is restored through charge transfer from Nb-d^1 to Sn-5*s* orbitals, in agreement with our computations (Figure 3). Therefore, due to the charge transfer from SNO to BSO across the interface, charge depletion in near-interface SNO layers is expected, in excellent agreement with the reduced real space charge density amplitude near the BSO/SNO interface (Figure 2).

To experimentally study the DFT predicted charge transfer, and Sn^{4+} to Sn^{3+} reduction, BSO/SNO heterostructures were synthesized and characterized as described above. The two heterostructures are represented schematically in Figure 4a. The Sn-3*d* core level spectra for an uncapped sample and a SHO-capped sample in reference to the plasma-cleaned BSO on the Nb:STO substrate at 45 and 70° photoelectron emission angles are shown in Figure 4b. In an uncapped sample, ARXPS measurements of the Sn-3*d* core level at a shallower angle show a more prominent additional shoulder at lower binding energy compared to the 45° orientation. This extra shoulder is assigned to Sn^{3+} associated with charge transfer-induced Sn^{4+} reduction. Additionally, Sn-$3d_{5/2}$ core level deconvolution of a substrate along with SHO-capped sample grown on is carried out using the same constraints as for the uncapped sample. A plasma-cleaned bare BSO on the Nb:STO substrate shows no secondary peak at lower binding energy. To quantify this lower oxidation state associated with Sn, the Sn-$3d_{5/2}$ core level of the uncapped sample is deconvoluted by constraining a second component with the same full width at half-maximum as the Sn^{4+} component and at 1.75 eV lower binding energy than the Sn^{4+} component, as shown in Figure 4b, for 70° photoelectron emission angle.

Deconvolution of a capped sample demonstrates that the SHO capping has increased the area of the Sn^{3+} shoulder at lower binding energy compared to the uncapped sample at 45° emission. This result suggests that the capping of the SNO film surface is a key ingredient for SNO to donate mobile charge carriers to the BSO interface layer. These free electrons fill Sn-5*s* states as reported previously,[11,47] improve charge carrier mobility, and facilitate 2DEG formation. For the purpose of estimating charge transfer, however, we choose to focus on the uncapped sample for better depth resolution into the BSO layer.

The Sn^{3+} abundance in the uncapped sample was obtained by deconvoluting the Sn-$3d_{5/2}$ core level as a function of photoelectron emission angle collected from 45 to 70° at an interval of 5° in ARXPS analysis (Figure 5). As the

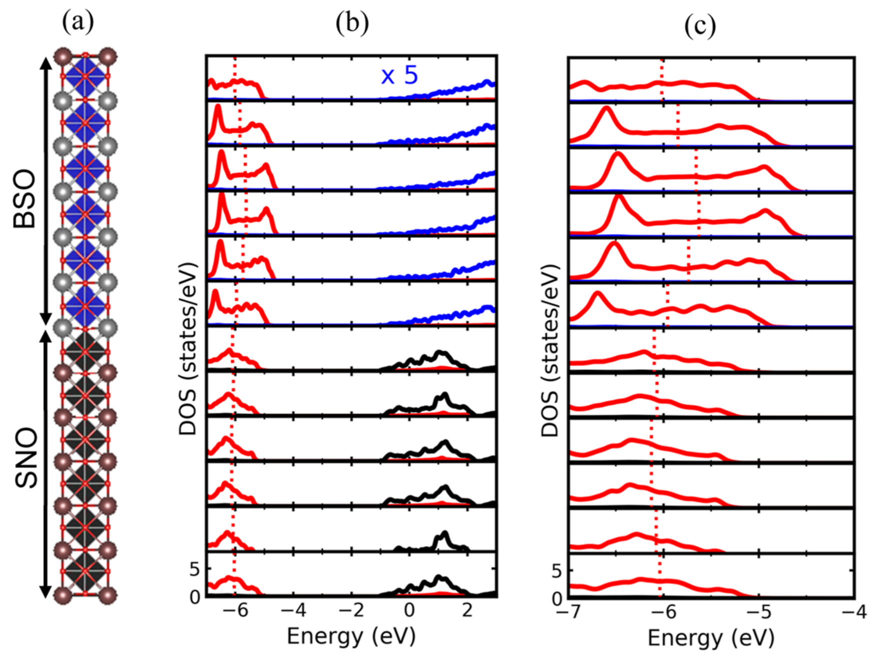

Figure 3. (BSO)6/(SNO)6 heterostructure: (a) atomic structure, blue and black octahedra correspond to Sn and Nb coordination, respectively. (b) Layer-projected partial density of states (pdos) of O-2*p* (red), Sn-5*s* (blue), and Nb-4*d* (black). The pdos Sn-5*s* (blue) is zoomed in by 5 times, (c) pdos of O-2*p* taken between 7 and 4 eV below the Fermi energy. The vertical dotted line (red) is the center-of-mass of O-2*p*, relative to the Fermi energy at E = 0 eV.

https://doi.org/10.1021/acsami.2c12195
ACS Appl. Mater. Interfaces 2022, 14, 45025−45031

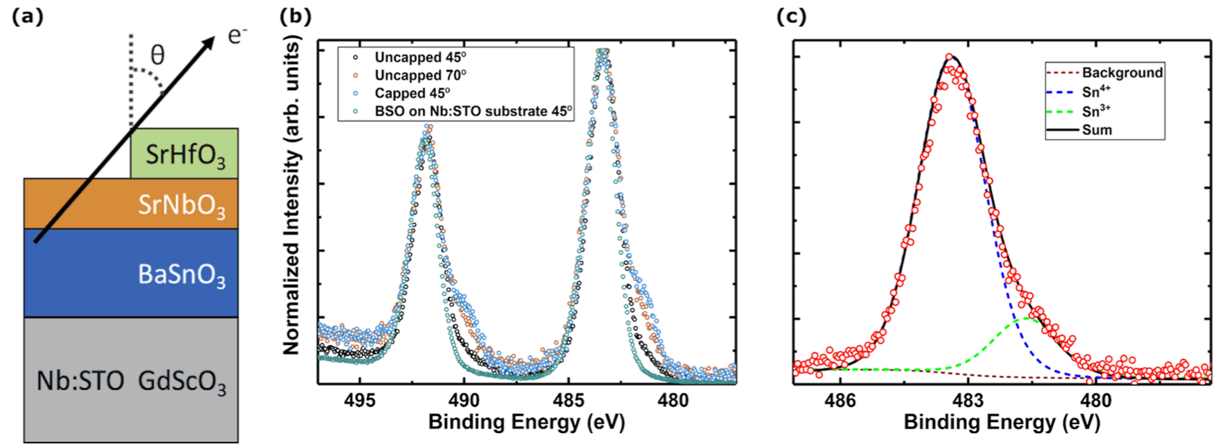

Figure 4. (a) Schematic of heterostructures studied by ARXPS including emission angle θ, showing an uncapped sample on Nb:STO and capped sample on $GdScO_3$; (b) Sn-3*d* core level for the uncapped sample at $\theta = 45°$ and $\theta = 70°$ emission angles and SHO-capped sample substrate at $\theta = 45°$, and (c) Sn-$3d_{5/2}$ core level of an uncapped sample deconvolved for a 70° photoelectron emission angle.

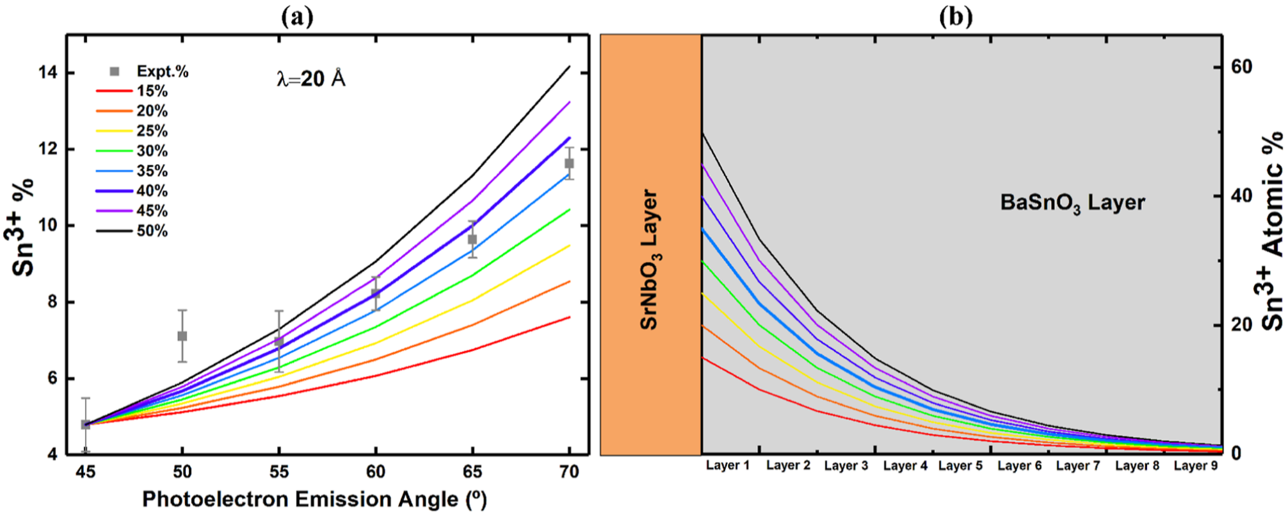

Figure 5. (a) Experimental Sn^{3+} peak area ratio as a function of photoelectron emission angle scatter plot and model fitted for different concentrations and (b) Sn^{3+} atomic percentage decay model as a function of BSO thickness.

photoelectron emission angle becomes shallower, an increasing trend of Sn^{3+} concentration in the BSO layer is observed. This result shows that the Sn^{3+} charge state is greater toward the surface of the heterostructure, consistent with an accumulation of electrons at the BSO/SNO interface. Such measurements have also been employed in the past for a variety of oxide heterostructures to examine cation intermixing and electron accumulation at an interface from charge transfer.[48] More sophisticated modeling of the electron concentration within each unit cell of the BSO film below the interface can also be used to estimate the electron density within the BSO layer.

By assuming a reduction in the electron concentration of 33% per BSO unit cell moving away from the interface, which mimics the DFT results above, we can derive a model to estimate the Sn^{3+} distribution in BSO (Figure 5b). Due to the high degree of Sn-5*s* states in BSO, a significantly greater electron diffusion into the film would be expected in comparison to the more localized transition metal d-states that are commonly studied in oxide interfaces. We assume an inelastic mean free path (IMFP) of 20 Å, suitable for the kinetic energy of Sn-3*d* electrons passing through the SNO layer and a BSO layer of thickness 40 Å (9-unit cells). This model allows us to predict the contributions of electrons at various depths within BSO to the ARXPS experimental data. An analogous model was employed previously to estimate cation intermixing in $LaCrO_3/SrTiO_3$ superlattices.[49] This analysis shows that a model with ∼35−40% Sn^{3+} concentration at the BSO/SNO interface fits well with the ARXPS results. However, lab-based ARXPS is relatively insensitive to electron diffusion into BSO, which merits further study using advanced techniques such as hard X-ray photoemission.[50,51] We emphasize that these results rely on several assumptions and are not a unique "best-fit" to the ARXPS data but provide an estimate of the charge transfer from SNO to BSO that accounts for electron diffusion into the BSO layer.

Taking 4.1 Å as a lattice parameter for the BSO cubic structure, we have estimated the volume electron density and sheet carrier concentration at the interface BSO layer for 35% Sn^{3+} electronic states. An estimated electron density of 4×10^{21} cm^{-3} in the interfacial BSO layer of BSO/SNO interface is significantly higher than other reports for La-doped BSO films,[17,51] La-doped BSO single crystals,[17,52] and oxygen-deficient BSO films[53] by at least a factor of 4 in all cases. The sheet electron concentration estimated from the ACBN0

https://doi.org/10.1021/acsami.2c12195
ACS Appl. Mater. Interfaces 2022, 14, 45025−45031

model is ~0.4×10^{14} cm^{-2} at the interface, which also agrees semi-quantitatively with the sheet electron concentration estimated from the ARXPS model (>1.8×10^{14} cm^{-2}) for only the interfacial layer of the BSO film. This charge carrier value as estimated from the ARXPS model is roughly an order of magnitude larger than those reported for $LaInO_3$/BSO polar/non-polar interfaces[47,54,55] and ~30× larger than modulation-doped La:$SrSnO_3$/BSO heterostructures.[50] Differences between theory and experiment are attributed to the larger BSO band gap (3.6 eV) in the ACBN0 computations, in comparison to the experimental band gap of ~3.1 eV.[56] This difference leads to an underestimate of the charge transfer from SNO to BSO. Following ref 19, we estimate that correcting for the 0.5 eV overestimation of the (bulk) BSO band gap could lead to an underestimated charge transfer by an order of magnitude. Therefore, charge carrier densities obtained from our computations and experiments are consistent. Additional variation could occur due to out-diffusion of Sn cations into the SNO that would complicate the ARXPS model. Finally, while we cannot rule out the presence of some growth-induced oxygen vacancies at the interface, we do not believe that our results can be explained solely based on oxygen vacancies (for details see the Supporting Information).

Future studies in this area should focus on determination of transport behavior and carrier dynamics in these heterostructures using models that account for the parallel conduction pathways within the BSO 2DEG and the partially electron-depleted SNO layer. The models developed for charge transfer provide an estimate of the expected sheet carrier concentration within BSO, but decoupling the contributions of BSO and SNO to transport behavior is likely to prove challenging. Efforts have been made to decouple the transport contributions from distinct layers in similar La/BSO,[50] $SrTaO_3$/STO,[57] and SNO/STO heterostructures,[58] but care must be taken to account for the surface instability of SNO in these models. We suggest that THz spectroscopy studies may provide a promising avenue for further examination of these 2D electronic systems.[59] Future studies could also explore the growth of SNO on thicker BSO layers such as single-crystal BSO[52] or on films grown on a lattice matched substrate such as Ba_2ScNbO_6,[60] which would open up easier pathways for device integration.

CONCLUSIONS

In conclusion, Hubbard-U-augmented DFT computations show that BSO/SNO superlattices exhibit charge transfer and high mobility for 2DEG formation in the BSO layer. For thin heterostructures, the CBM is dominated by Sn-5*s* bands and located well below the Fermi energy. The CBM corresponds to a low effective mass of ~0.10 m_0 and varies by less than ~6% for thin heterostructures and remains very similar to high-mobility bulk BSO. The CBM in the (BSO)6/(SNO)6 heterostructure shows the highest CBM suppression below the Fermi energy, ~1.2 eV, corresponding to a high electron density of ~10^{21} cm^{-3}. Thinner heterostructures show less pronounced CBM suppression. In contrast, the CBM in thicker heterostructures is dominated by Nb-4*d* electronic states. BSO/SNO heterostructures grown by hMBE confirm the expected charge transfer, based on in situ XPS analysis of the Sn-3*d* core level peak. The quantitative analysis of the ARXPS results shows that the capping layer of SHO enhances charge transfer across the BSO/SNO interface. The interfacial BSO electron density from ARXPS is ~4×10^{21} cm^{-3}, in a semi-quantitative agreement with our ACBN0 predicted electron density of ~10^{21} cm^{-3}. Integration across the depth of the film produces a total charge density in a BSO layer of ~10^{14} cm^{-2}. Therefore, BSO/SNO heterostructures are promising materials for hosting a high mobility 2DEG and the study of their emergent properties.

ASSOCIATED CONTENT

Supporting Information

The Supporting Information is available free of charge at https://pubs.acs.org/doi/10.1021/acsami.2c12195.

Computational details, experimental methods, DFT results and discussion, experimental results and discussions (PDF)

AUTHOR INFORMATION

Corresponding Authors

Ryan Comes − *Department of Physics, Auburn University, Auburn, Alabama 36849, United States;* orcid.org/0000-0002-5304-6921; Email: ryan.comes@auburn.edu

Boris Kiefer − *Department of Physics, New Mexico State University, Las Cruces, New Mexico 88003-8001, United States;* orcid.org/0000-0003-0242-3165; Email: bkiefer@nmsu.edu

Authors

Sharad Mahatara − *Department of Physics, New Mexico State University, Las Cruces, New Mexico 88003-8001, United States;* orcid.org/0000-0003-1604-0966

Suresh Thapa − *Department of Physics, Auburn University, Auburn, Alabama 36849, United States*

Hanjong Paik − *Platform for the Accelerated Realization, Analysis, and Discovery of Interface Materials (PARADIM), Cornell University, Ithaca, New York 14853, United States; School of Electrical & Computer Engineering, University of Oklahoma, Norman, Oklahoma 73019, United States*

Complete contact information is available at: https://pubs.acs.org/10.1021/acsami.2c12195

Author Contributions

S.M. and S.T. contributed equally to this work. The manuscript was written through contributions of all authors. All authors have given approval to the final version of the manuscript.

Notes

The authors declare no competing financial interest.

ACKNOWLEDGMENTS

The authors thank Marcelo Kuroda of Auburn University for helpful discussions. B.K. and S.M. would like to acknowledge computing support by the Extreme Science and Engineering Discovery Environment (XSEDE) resource Stampede2 at TACC through allocation TG-DMR110093. S.T. and R.B.C. gratefully acknowledge support from the Air Force Office of Scientific Research under award number FA9550-20-1-0034 and Alabama EPSCoR-GRSP Fellowship. H.P. acknowledges partial support through the National Science Foundation (Platform for the Accelerated Realization, Analysis, and Discovery of Interface Materials (PARADIM)) under Cooperative Agreement no. DMR-2039380.

ABBREVIATIONS

2DEG, two-dimensional electron gas

https://doi.org/10.1021/acsami.2c12195
ACS Appl. Mater. Interfaces 2022, 14, 45025−45031

LAO, $LaAlO_3$
STO, $SrTiO_3$
BSO, $BaSnO_3$
SNO, $SrNbO_3$
DFT, density functional theory
CBM, conduction band minimum
VBM, valence band maximum
CM, center-of-mass
XPS, X-ray photoelectron spectroscopy
ARXPS, angle-resolved XPS
hMBE, hybrid molecular beam epitaxy

REFERENCES

(1) Reyren, N.; Thiel, S.; Caviglia, A. D.; Kourkoutis, L. F.; Hammerl, G.; Richter, C.; Schneider, C. W.; Kopp, T.; Rüetschi, A.-S.; Jaccard, D.; Gabay, M.; Muller, D. A.; Triscone, J.-M.; Mannhart, J. Superconducting Interfaces between Insulating Oxides. *Science* **2007**, *317*, 1196−1199.

(2) Ohtomo, A.; Hwang, H. Y. A High-Mobility Electron Gas at the $LaAlO_3/SrTiO_3$ Heterointerface. *Nature* **2004**, *427*, 423−426.

(3) Lim, S.-G.; Kriventsov, S.; Jackson, T. N.; Haeni, J. H.; Schlom, D. G.; Balbashov, A. M.; Uecker, R.; Reiche, P.; Freeouf, J. L.; Lucovsky, G. Dielectric Functions and Optical Bandgaps of High-K Dielectrics for Metal-Oxide-Semiconductor Field-Effect Transistors by Far Ultraviolet Spectroscopic Ellipsometry. *J. Appl. Phys.* **2002**, *91*, 4500−4505.

(4) Higuchi, T.; Tsukamoto, T.; Sata, N.; Ishigame, M.; Tezuka, Y.; Shin, S. Electronic Structure of p-Type $SrTiO_3$ by Photoemission Spectroscopy. *Phys. Rev. B: Condens. Matter Mater. Phys.* **1998**, *57*, 6978−6983.

(5) Thiel, S.; Hammerl, G.; Schmehl, A.; Schneider, C. W.; Mannhart, J. Tunable Quasi-Two-Dimensional Electron Gases in Oxide Heterostructures. *Science* **2006**, *313*, 1942−1945.

(6) Ohtomo, A.; Muller, D. A.; Grazul, J. L.; Hwang, H. Y. Artificial Charge-Modulation in Atomic-Scale Perovskite Titanate Superlattices. *Nature* **2002**, *419*, 378−380.

(7) Lu, H.-L.; Liao, Z.-M.; Zhang, L.; Yuan, W.-T.; Wang, Y.; Ma, X.-M.; Yu, D.-P. Reversible Insulator-Metal Transition of $LaAlO_3/SrTiO_3$ Interface for Nonvolatile Memory. *Sci. Rep.* **2013**, *3*, 2870.

(8) Weston, L.; Cui, X. Y.; Ringer, S. P.; Stampfl, C. Density-Functional Prediction of a Surface Magnetic Phase in $SrTiO_{(3)}/LaAlO_{(3)}$ Heterostructures Induced by Al Vacancies. *Phys. Rev. Lett.* **2014**, *113*, 186401.

(9) Kalisky, B.; Spanton, E. M.; Noad, H.; Kirtley, J. R.; Nowack, K. C.; Bell, C.; Sato, H. K.; Hosoda, M.; Xie, Y.; Hikita, Y.; Woltmann, C.; Pfanzelt, G.; Jany, R.; Richter, C.; Hwang, H. Y.; Mannhart, J.; Moler, K. A. Locally Enhanced Conductivity Due to the Tetragonal Domain Structure in $LaAlO_3/SrTiO_3$ Heterointerfaces. *Nat. Mater.* **2013**, *12*, 1091−1095.

(10) Nazir, S.; Cheng, J.; Behtash, M.; Luo, J.; Yang, K. Interface Energetics and Charge Carrier Density Amplification by Sn-Doping in $LaAlO_3/SrTiO_3$ Heterostructure. *ACS Appl. Mater. Interfaces* **2015**, *7*, 14294−14302.

(11) Xiang, X.; Qiao, L.; Xiao, H. Y.; Gao, F.; Zu, X. T.; Li, S.; Zhou, W. L. Effects of Surface Defects on Two-Dimensional Electron Gas at $NdAlO_3/SrTiO_3$ Interface. *Sci. Rep.* **2014**, *4*, 5477.

(12) Xu, P.; Ayino, Y.; Cheng, C.; Pribiag, V. S.; Comes, R. B.; Sushko, P. V.; Chambers, S. A.; Jalan, B. Predictive Control over Charge Density in the Two-Dimensional Electron Gas at the Polar-Nonpolar$NdTiO_3/SrTiO_3$ Interface. *Phys. Rev. Lett.* **2016**, *117*, 106803.

(13) Biscaras, J.; Hurand, S.; Feuillet-Palma, C.; Rastogi, A.; Budhani, R. C.; Reyren, N.; Lesne, E.; Lesueur, J.; Bergeal, N. Limit of the Electrostatic Doping in Two-Dimensional Electron Gases of $LaXO_3$(X = Al, Ti)/$SrTiO_3$. *Sci. Rep.* **2014**, *4*, 6788.

(14) Verma, A.; Kajdos, A. P.; Cain, T. A.; Stemmer, S.; Jena, D. Intrinsic Mobility Limiting Mechanisms in Lanthanum-Doped Strontium Titanate. *Phys. Rev. Lett.* **2014**, *112*, 216601.

(15) Prakash, A.; Xu, P.; Faghaninia, A.; Shukla, S.; Ager, J. W.; Lo, C. S.; Jalan, B. Wide Bandgap $BaSnO_3$ Films with Room Temperature Conductivity Exceeding 104 SCm^{-1}. *Nat. Commun.* **2017**, *8*, 15167.

(16) Paik, H.; Chen, Z.; Lochocki, E.; Seidner, H. A.; Verma, A.; Tanen, N.; Park, J.; Uchida, M.; Shang, S.; Zhou, B.-C.; Brützam, M.; Uecker, R.; Liu, Z.-K.; Jena, D.; Shen, K. M.; Muller, D. A.; Schlom, D. G. Adsorption-Controlled Growth of La-Doped $BaSnO_3$ by Molecular-Beam Epitaxy. *APL Mater.* **2017**, *5*, 116107.

(17) Kim, H. J.; Kim, U.; Kim, H. M.; Kim, T. H.; Mun, H. S.; Jeon, B.-G.; Hong, K. T.; Lee, W.-J.; Ju, C.; Kim, K. H.; Char, K. High Mobility in a Stable Transparent Perovskite Oxide. *Appl. Phys. Express* **2012**, *5*, 061102.

(18) Krishnaswamy, K.; Himmetoglu, B.; Kang, Y.; Janotti, A.; Van de Walle, C. G. First-Principles Analysis of Electron Transport in $BaSnO_3$. *Phys. Rev. B: Condens. Matter Mater. Phys.* **2017**, *95*, 205202. . arXiv [cond-mat.mtrl-sci]

(19) Krishnaswamy, K.; Bjaalie, L.; Himmetoglu, B.; Janotti, A.; Gordon, L.; Van de Walle, C. G. $BaSnO_3$ as a Channel Material in Perovskite Oxide Heterostructures. *Appl. Phys. Lett.* **2016**, *108*, 083501.

(20) Kc, S.; Rowberg, A. J. E.; Weston, L.; Van de Walle, C. G. First-Principles Study of Antisite Defects in Perovskite Stannates. *J. Appl. Phys.* **2019**, *126*, 195701.

(21) Bigi, C.; Orgiani, P.; Sławińska, J.; Fujii, J.; Irvine, J. T.; Picozzi, S.; Panaccione, G.; Vobornik, I.; Rossi, G.; Payne, D.; Borgatti, F. Direct Insight into the Band Structure of $SrNbO_3$. *Phys. Rev. Mater.* **2020**, *4*, 025006.

(22) Thapa, S.; Provence, S. R.; Gemperline, P. T.; Matthews, B. E.; Spurgeon, S. R.; Battles, S. L.; Heald, S. M.; Kuroda, M. A.; Comes, R. B. Surface Stability of SrNbO3+δ Grown by Hybrid Molecular Beam Epitaxy. *APL Materials* **2022**, *10*, 091112.

(23) Agapito, L. A.; Curtarolo, S.; Buongiorno Nardelli, M. Reformulation Of DFT+U as a Pseudohybrid Hubbard Density Functional for Accelerated Materials Discovery. *Phys. Rev. X.* **2015**, *5*, 011006.

(24) Supka, A. R.; Lyons, T. E.; Liyanage, L.; D'Amico, P.; Al Rahal Al Orabi, R.; Mahatara, S.; Gopal, P.; Toher, C.; Ceresoli, D.; Calzolari, A.; Curtarolo, S.; Nardelli, M. B.; Fornari, M. AFLOWπ: A Minimalist Approach to High-Throughput Ab Initio Calculations Including the Generation of Tight-Binding Hamiltonians. *Comput. Mater. Sci.* **2017**, *136*, 76−84.

(25) Mahatara, S.; Kiefer, B. Does β-PbO_2 Harbor Topological States? *J. Phys.: Condens. Matter* **2020**, *32*, 255504.

(26) Mahatara, S.; Kiefer, B. Layer Dependent Magnetism and Topology in Monolayer and Bilayers ReX 3 (X= Br, I). *J. Phys.: Condens. Matter* **2021**, *33*, 455801.

(27) Giannozzi, P.; Andreussi, O.; Brumme, T.; Bunau, O.; Buongiorno Nardelli, M.; Calandra, M.; Car, R.; Cavazzoni, C.; Ceresoli, D.; Cococcioni, M.; Colonna, N.; Carnimeo, I.; Dal Corso, A.; de Gironcoli, S.; Delugas, P.; DiStasio, R. A., Jr; Ferretti, A.; Floris, A.; Fratesi, G.; Fugallo, G.; Gebauer, R.; Gerstmann, U.; Giustino, F.; Gorni, T.; Jia, J.; Kawamura, M.; Ko, H.-Y.; Kokalj, A.; Küçükbenli, E.; Lazzeri, M.; Marsili, M.; Marzari, N.; Mauri, F.; Nguyen, N. L.; Nguyen, H.-V.; Otero-de-la-Roza, A.; Paulatto, L.; Poncé, S.; Rocca, D.; Sabatini, R.; Santra, B.; Schlipf, M.; Seitsonen, A. P.; Smogunov, A.; Timrov, I.; Thonhauser, T.; Umari, P.; Vast, N.; Wu, X.; Baroni, S. Advanced Capabilities for Materials Modelling with Quantum ESPRESSO. *J. Phys.: Condens. Matter* **2017**, *29*, 465901.

(28) Giannozzi, P.; Baseggio, O.; Bonfà, P.; Brunato, D.; Car, R.; Carnimeo, I.; Cavazzoni, C.; de Gironcoli, S.; Delugas, P.; Ferrari Ruffino, F.; Ferretti, A.; Marzari, N.; Timrov, I.; Urru, A.; Baroni, S. Quantum ESPRESSO toward the Exascale. *J. Chem. Phys.* **2020**, *152*, 154105.

(29) Lee, S.; Wang, H.; Gopal, P.; Shin, J.; Jaim, H. M. I.; Zhang, X.; Jeong, S.-Y.; Usanmaz, D.; Curtarolo, S.; Fornari, M.; Buongiorno Nardelli, M.; Takeuchi, I. Systematic Band Gap Tuning of $BaSnO_3$ via Chemical Substitutions: The Role of Clustering in Mixed-Valence Perovskites. *Chem. Mater.* **2017**, *29*, 9378−9385.

(30) Blöchl, P. E. Projector Augmented-Wave Method. *Phys. Rev. B: Condens. Matter Mater. Phys.* **1994**, *50*, 17953−17979.

(31) Dal Corso, A. Pseudopotentials Periodic Table: From H to Pu. *Comput. Mater. Sci.* **2014**, *95*, 337−350.

(32) Perdew, J. P.; Burke, K.; Ernzerhof, M. Generalized Gradient Approximation Made Simple. *Phys. Rev. Lett.* **1996**, *77*, 3865−3868.

(33) May, K. J.; Kolpak, A. M. Improved Description of Perovskite Oxide Crystal Structure and Electronic Properties Using Self-Consistent Hubbard U Corrections from ACBN0. *Phys. Rev. B: Condens. Matter Mater. Phys.* **2020**, *101*, 165117.

(34) Aggoune, W.; Eljarrat, A.; Nabok, D.; Irmscher, K.; Zupancic, M.; Galazka, Z.; Albrecht, M.; Koch, C.; Draxl, C. A Consistent Picture of Excitations in Cubic $BaSnO_3$ Revealed by Combining Theory and Experiment. *Commun. Mater.* **2022**, *3*, 12.

(35) Park, Y.; Roth, J.; Oka, D.; Hirose, Y.; Hasegawa, T.; Paul, A.; Pogrebnyakov, A.; Gopalan, V.; Birol, T.; Engel-Herbert, R. $SrNbO_3$ as a Transparent Conductor in the Visible and Ultraviolet Spectra. *Commun. Phys.* **2020**, *3*, 102.

(36) Mizoguchi, H.; Chen, P.; Boolchand, P.; Ksenofontov, V.; Felser, C.; Barnes, P. W.; Woodward, P. M. Electrical and Optical Properties of Sb-Doped $BaSnO_3$. *Chem. Mater.* **2013**, *25*, 3858−3866.

(37) Garcia-Castro, A. C.; Ma, Y.; Romestan, Z.; Bousquet, E.; Cen, C.; Romero, A. H. Engineering of Ferroic Orders in Thin Films by Anionic Substitution. *Adv. Funct. Mater.* **2022**, *32*, 2107135. arXiv [cond-mat.mtrl-sci]

(38) Prakash, A.; Wang, T.; Choudhary, R.; Haugstad, G.; Gladfelter, W. L.; Jalan, B. Precursor Selection in Hybrid Molecular Beam Epitaxy of Alkaline-Earth Stannates. *J. Vac. Sci. Technol., A* **2020**, *38*, 063410.

(39) Paudel, T. R.; Tsymbal, E. Y. Prediction of a Mobile Two-Dimensional Electron Gas at the $LaScO_3/BaSnO_3$ (001) Interface. *Phys. Rev. B: Condens. Matter Mater. Phys.* **2017**, *96*, 245423.

(40) Zha, X.-H.; Zhou, J.; Zhou, Y.; Huang, Q.; He, J.; Francisco, J. S.; Luo, K.; Du, S. Promising Electron Mobility and High Thermal Conductivity in Sc_2CT_2 (T = F, OH) MXenes. *Nanoscale* **2016**, *8*, 6110−6117.

(41) Janotti, A.; Bjaalie, L.; Gordon, L.; Van de Walle, C. G. Controlling the Density of the 2DEG at the SrTiO3/LaAlO3 Interface. *Phys. Rev. B: Condens. Matter Mater. Phys.* **2012**, *86*, 241108. arXiv [cond-mat.mtrl-sci]

(42) Wang, Y.; Comes, R. B.; Kittiwatanakul, S.; Wolf, S. A.; Lu, J. Epitaxial Niobium Dioxide Thin Films by Reactive-Biased Target Ion Beam Deposition. *J. Vac. Sci. Technol., A* **2015**, *33*, 021516.

(43) Baer, D. R.; Artyushkova, K.; Richard Brundle, C. R.; Castle, J. E.; Engelhard, M. H.; Gaskell, K. J.; Grant, J. T.; Haasch, R. T.; Linford, M. R.; Powell, C. J.; Shard, A. G.; Sherwood, P. M. A.; Smentkowski, V. S. Practical Guides for X-Ray Photoelectron Spectroscopy (XPS): First Steps in Planning, Conducting and Reporting XPS Measurements. *J. Vac. Sci. Technol., A* **2019**, *37*, 031401.

(44) Fairley, N.; Carrick, A. *Recipes for XPS Data Processing*; Acolyte Science, 2005.

(45) Pentcheva, R.; Huijben, M.; Otte, K.; Pickett, W. E.; Kleibeuker, J. E.; Huijben, J.; Boschker, H.; Kockmann, D.; Siemons, W.; Koster, G.; Zandvliet, H. J. W.; Rijnders, G.; Blank, D. H. A.; Hilgenkamp, H.; Brinkman, A. Parallel Electron-Hole Bilayer Conductivity from Electronic Interface Reconstruction. *Phys. Rev. Lett.* **2010**, *104*, 166804. arXiv [cond-mat.mtrl-sci]

(46) Zhong, Z.; Hansmann, P. Band Alignment and Charge Transfer in Complex Oxide Interfaces. *Phys. Rev. X* **2017**, *7*, 011023.

(47) Shin, J.; Kim, Y. M.; Park, C.; Char, K. Remote Doping of the Two-Dimensional-Electron-Gas State at the $LaInO_3/BaSnO_3$ Polar Interface. *Phys. Rev. Appl.* **2020**, *13*, 064066.

(48) Thapa, S.; Paudel, R.; Blanchet, M. D.; Gemperline, P. T.; Comes, R. B. Probing Surfaces and Interfaces in Complex Oxide Films via in Situ X-Ray Photoelectron Spectroscopy. *J. Mater. Res.* **2021**, *36*, 26−51.

(49) Comes, R. B.; Spurgeon, S. R.; Kepaptsoglou, D. M.; Engelhard, M. H.; Perea, D. E.; Kaspar, T. C.; Ramasse, Q. M.; Sushko, P. V.; Chambers, S. A. Probing the Origin of Interfacial Carriers in $SrTiO_3$−$LaCrO_3$ Superlattices. *Chem. Mater.* **2017**, *29*, 1147−1155.

(50) Prakash, A.; Quackenbush, N. F.; Yun, H.; Held, J.; Wang, T.; Truttmann, T.; Ablett, J. M.; Weiland, C.; Lee, T.-L.; Woicik, J. C.; Mkhoyan, K. A.; Jalan, B. Separating Electrons and Donors in $BaSnO_3$ via Band Engineering. *Nano Lett.* **2019**, *19*, 8920−8927.

(51) Lebens-Higgins, Z.; Scanlon, D. O.; Paik, H.; Sallis, S.; Nie, Y.; Uchida, M.; Quackenbush, N. F.; Wahila, M. J.; Sterbinsky, G. E.; Arena, D. A.; Woicik, J. C.; Schlom, D. G.; Piper, L. F. J. Direct Observation of Electrostatically Driven Band Gap Renormalization in a Degenerate Perovskite Transparent Conducting Oxide. *Phys. Rev. Lett.* **2016**, *116*, 027602.

(52) Terry, R. J.; Combs, N.; McMillen, C. D.; Stemmer, S.; Kolis, J. W. Hydrothermal Growth of $BaSnO_3$ Single Crystals for Wide Bandgap Applications. *J. Cryst. Growth* **2020**, *536*, 125529.

(53) Ganguly, K.; Ambwani, P.; Xu, P.; Jeong, J. S.; Mkhoyan, K. A.; Leighton, C.; Jalan, B. Structure and Transport in High Pressure Oxygen Sputter-Deposited $BaSnO_{3-\delta}$. *APL Mater.* **2015**, *3*, 062509.

(54) Kim, Y.; Kim, S.; Cho, H.; Kim, Y. M.; Ohta, H.; Char, K. Transport Properties of the $LaInO_3/BaSnO_3$ Interface Analyzed by Poisson-Schrödinger Equation. *Phys. Rev. Appl.* **2022**, *17*, 014031.

(55) Cho, H.; Song, D.; Kim, Y.; Kim, B.; Char, K. High-Mobility Field-Effect Transistor Using 2-Dimensional Electron Gas at the $LaScO_3/BaSnO_3$ Interface. *ACS Appl. Electron. Mater.* **2022**, *4*, 356−366.

(56) Chambers, S. A.; Kaspar, T. C.; Prakash, A.; Haugstad, G.; Jalan, B. Band Alignment at Epitaxial $BaSnO_3/SrTiO_3$(001) and $BaSnO_3/LaAlO_3$(001) Heterojunctions. *Appl. Phys. Lett.* **2016**, *108*, 152104.

(57) Zhang, J.; Pai, Y.-Y.; Lapano, J.; Mazza, A. R.; Lee, H. N.; Moore, R. G.; Lawrie, B. J.; Ward, T. Z.; Eres, G.; Cooper, V. R.; Brahlek, M. Design and Realization of Ohmic and Schottky Interfaces for Oxide Electronics. *Small Sci.* **2022**, *2*, 2100087.

(58) Zhang, J.; Ok, J. M.; Pai, Y.-Y.; Lapano, J.; Skoropata, E.; Mazza, A. R.; Li, H.; Huon, A.; Yoon, S.; Lawrie, B.; Brahlek, M.; Ward, T. Z.; Eres, G.; Miao, H.; Lee, H. N. Extremely Large Magnetoresistance in High-Mobility $SrNbO_3/SrTiO_3$ Heterostructures. *Phys. Rev. B: Condens. Matter Mater. Phys.* **2021**, *104*, L161404.

(59) Arezoomandan, S.; Prakash, A.; Chanana, A.; Yue, J.; Mao, J.; Blair, S.; Nahata, A.; Jalan, B.; Sensale-Rodriguez, B. THz Characterization and Demonstration of Visible-Transparent/Terahertz-Functional Electromagnetic Structures in Ultra-Conductive La-Doped $BaSnO_3$ Films. *Sci. Rep.* **2018**, *8*, 3577.

(60) Guguschev, C.; Klimm, D.; Brützam, M.; Gesing, T. M.; Gogolin, M.; Paik, H.; Dittmar, A.; Fratello, V. J.; Schlom, D. G. Single Crystal Growth and Characterization of Ba_2ScNbO_6 − A Novel Substrate for $BaSnO_3$ Films. *J. Cryst. Growth* **2019**, *528*, 125263.

https://doi.org/10.1021/acsami.2c12195
ACS Appl. Mater. Interfaces 2022, 14, 45025−45031